Near-threshold electron-impact doubly differential cross sections for the ionization of argon and krypton

Brent R. Yates and Murtadha A. Khakoo
Department of Physics, California State University Fullerton, Fullerton, California 92831, USA
(Received 13 January 2011; published 26 April 2011)

We present normalized doubly differential cross sections (DDCS's) for the near-threshold, electron-impact single ionization of argon and krypton, similar to those taken earlier for Ne and Xe [Yates *et al.*, J. Phys. B **42**, 095206 (2009)]. The Ar measurements were taken at incident energies of 17, 18, 20, and 30 eV while the Kr measurements were taken at 15, 16, 17.5, and 20 eV. The DDCS scattering angles range from 15° to 120°. The differential data are initially normalized to available experimental cross sections for excitation of the ground np^6 to the $np^5(n+1)s$ excited states of the noble gas and, after integration, to well-established experimental total ionization cross sections of Rapp and Englander-Golden [J. Chem. Phys. **43**, 1464 (1965)].

DOI: 10.1103/PhysRevA.83.042712 PACS number(s): 34.80.Dp, 25.30.Dh

I. INTRODUCTION

The use of rare gases as buffers in industrial plasmas has demonstrated the need for accurately known electron-impact cross sections for these targets at low energies above the threshold for excitation and ionization. Recently, with the advent of large computers incorporating sophisticated collision models such as the exterior scaling model [1] as well as the convergent close-coupling model [2], it became possible to accurately model the ionization of H [1,2] and He [3,4]. We note here that in the ionization of H, the ion core is a proton monopole, whereas for He the core is a 1*s* polarizable dipole, i.e., adding on another level of complexity. Methods of dealing with the ionized 1*s* core in the electron-impact ionization of He have been discussed by Horner *et al.* [4], who weighed the various schemes such as the polarized-core model. The rare gases pose much more difficult targets to model since the ionized core is an np^5 shell and the consequent ionized $^2P_{1/2}$ core displays a strongly interactive permanent dipole moment. In the past, using electron-energy-loss spectroscopy, we have measured doubly differential cross sections (DDCS's) for the ionization of H [5] and He [6]. The work was made possible with the help of a novel moveable source method [7] to accurately remove the background in the continuum part of the electron-energy-loss spectrum. This allowed for the expedient measurement of background concurrently with the signal plus background spectrum without interrupting the experimental setup. Using our moveable source method, we recently extended our DDCS measurements for Ne and Xe at incident electron energies (E_0) ranging from 1 eV above threshold up to the second-ionization potential [8]. In that work, we observed what we hypothesized was the dynamic role of the polarized Ne core in inhibiting forward slow-moving ionized electrons. We also noted that for E_0 significantly above the ionization potential (IP), our singly differential cross-section (SDCS) results were able to discern that the SDCS for ionization of Ne favored equal kinetic energy sharing by the outgoing two electrons while Xe favored unequal sharing, similar to H and He. At lower-E_0 values, our results showed the suppression of slow electrons being emitted in the forward-scattering direction, i.e., these electrons were being sucked back by the aligned polarized ionic core.

The low-energy electron-impact ionization of the rare gases plays an important role in the transport of electrons in rare-gas discharges [9], which has relevance in plasma applications, such as in the processing of semiconductor wafers and plasma tubes [10,11], where rare gases are most frequently used as buffer gases. The study of the electron-impact ionization of these targets is complicated by the dynamics in the change of the $np^6 \rightarrow np^5$ core configuration by the single-ionization process, viz.,

$$e^-(E_0,l) + X\left([np^6]\,n\,^1S_0\right) \rightarrow X^+\left([np^5]\,n\,^2P_{3/2,1/2}\right) + 2e^-(LS), \quad (1)$$

where X is the rare-gas target impacted by an electron with a plane wave (partial wave of the plane wave with the orbital angular momentum l) resulting in two receding electrons with total orbital and spin angular momenta (L,S) [12]. The resultant fine structure in the residual ion X^+, a spin-orbit-coupled P core and also its coupling with the receding electrons (one that depends on the total energy of these electrons), provides for a more complicated picture than the more studied case of helium. In the case of Ne, one expects the coupling to be dominantly LS coupling, whereas for Xe it is expected to be largely spin-orbit coupling. In our earlier work on Ne and Xe [4], we observed for Ne that the SDCS favored strong equal-energy sharing between the two outgoing electrons; whereas for Xe an unequal-energy sharing (to a less strong level than Ne) was preferred, similar to that for He. We noted that the total ionization cross section for Ne was (surprisingly) lower than He, at the same residual energy (E_R) above threshold, from the absolute measurements of Rapp and Englander-Golden [13]. We hypothesized that the strong polarization potential of the ionized core of Ne suppressed the ionization process for forward-scattered, low E_R electrons, thus reducing the total ionization cross section close to the ionization threshold. We were therefore motivated to extend our measurements in [8] to Ar and Kr to see which energy-sharing regimes these targets would progressively fall into. Another reason for investigating Ar was that it is the most often used buffer rare gas in plasma discharges, and more work has been done in electron-impact ionization of Ar than any rare gas.

Presently, the most recent near-threshold electron-impact work on the ionization of the noble gases was the (e,2e) triple

differential cross-section (TDCS) measurements of Nixon *et al.* [14] in the perpendicular plane, from 3 to 80 eV above the first IP for He, from 5 to 50 eV above the IP for Ne, from 2 to 50 eV for Ar and Kr, and from 2 to 70 eV for Xe. In this work, electrons of equal energy were detected, so, for example, for the impact energy of 5 eV above the IP of the target, 2.5 eV E_R electrons were detected. For He they observed that the equal-energy electrons were very strongly emitted at 180° difference angles (ϕ), in agreement with the Wannier post-collision interaction (PCI) theory at low incident energies as much as 10 eV above the ionization threshold, before non-180° ϕ are observed. At low energies, electron motions are strongly correlated, and mutual repulsion causes them to be scattered into opposite directions, i.e., favoring ϕ around 180°. This seems to somewhat corroborate what was seen in our group [6] in He, however with the difference that in the perpendicular plane, multiple scattering is involved to make electrons emerge in this plane. The maximum of the (e,2e) distributions at 180° ϕ also suggested PCI effects in theory to be dominant for He or H_2 [15,16]. H_2 is a system of interest for its two-center symmetry and was recently investigated using the reaction microscope by Ren *et al.* [17]. It is expected to be similar to He, except that H_2, being a diatomic system, will exhibit two-center interference effects found in diatomic targets (e.g., [18] recently for H_2 and [19] for N_2). In what was an extensive set of measurements on all rare gases near-threshold, Nixon *et al.* [14] observed that the ionization mechanism for Ne was similar to He at up to 10 eV above the ionization potential, with PCI effects dominant at these low energies. However, as the incident energy was raised beyond this, the two equal-energy electrons preferentially came out at non-180° difference angles, in fact with a dramatic minimum in the distribution at 180° ϕ. For Ar the situation was different from He and Ar, and the two equal-energy electrons preferred to be emitted at non-180° angles even close to threshold. For Kr, the symmetry of the (e,2e) distributions in ϕ is very similar to Ar, showing that PCI effects were present but not dominant. For Xe, the situation once again changes. Stronger non-180° ϕ distributions were observed near-threshold; this changed rapidly with incident energy, but stabilized to a 180°-centered distribution in ϕ at 40 eV above the IP. The Nixon *et al.* [14] measurements are the only (e,2e) measurements covering all the rare gases at close to threshold. The earlier (e,2e) work of Selles *et al.* [12], which was taken in-plane, was in the 0.5–2-eV range above threshold with equal sharing of the energy of ionized electrons at 0.25, 0.5, and 1 eV, and covered Ne, Ar, and Kr.

Near-threshold in-plane measurements in Ar were also recently taken by Rouvellou *et al.* [20] for incident energies of 2–40 eV above the IP. The equal-energy sharing electrons (from the experimental data) are not emitted at difference angles around 180°, although theory (distorted wave) shows a strong 180° difference angle peak, in disagreement with the experiment. The authors point out that the poor performance of the theory could be due to an incomplete treatment of PCI effects as well as not including the polarization potential in the post-collision channel. Recently, in-plane (e,2e) measurements in Ar at the higher E_0 value of 113.5 eV were taken by Stevenson and Lohmann [21] using a magnetic angle changer [22]. Mixed agreement with a distorted-wave-type calculation was observed, and the inclusion of PCI in the theory resulted in some improved agreement with experiment. However, these results showed that much improvement in theory is required to accommodate PCI, polarization, and relativistic effects for electron scattering from these targets.

To date, DDCS measurements for Ar and Kr are available only at high energies (240–1000 eV) by DuBois and co-workers [23–25]. For these measurements, there are no theoretical models to compare with. In [23,24], they also took DDCS measurements for these targets using positrons, and observed that there was less difference between the electron-impact and positron-impact DDCS's for Kr than for Ar. They suggested that this was due to the role of inner-shell ionization [24]. Many total-ionization cross-section measurements (TICS) for the rare gases have been carried out, such as those of Rapp and Englander-Golden [13] and others, which are summarized most recently in Rejoub *et al.* [26]. Rejoub *et al.* [26] call the work of [13] "the *de facto* standard" and observe excellent agreement with them throughout the E_0 range of [13], i.e., threshold to 1000 eV. The work of Rejoub *et al.* [26] extends that of [13] by providing a complete set of consistent absolute, partial ionization cross sections using an ingenious time-of-flight mass spectrometer coupled to their extended electron-target collision region. In most cases, the agreement between TICS measurements listed in [26] is very good.

We have focused our effort to obtain DDCS's from 1 eV above the IP threshold to near the second IP. In this region, the role of relativistic effects at energies below the second IP of these targets will be important in an effort to understand the role of nondipole, exchange, and spin-orbit interactions in the ionization, as well as the role of PCI. The post-collision effect of the core's $P_{1/2,3/2}$ dipole potential will play a major role in characterizing the emission of the ionized electrons, as was observed in [8]. The present measurements were carried out for Ar at E_0 values 17, 18, 20, and 30 eV (first IP = 15.758 eV and second IP = 27.626 eV) and 15, 16, 17.5, and 20 eV for Kr (first IP = 13.998 eV and second IP = 24.357 eV). Hence for Ar we exceeded the second IP, but for Kr we stayed below the second IP. The DDCS scattering angles range from 10° to 120°. E_R values of as low as 0.3 eV were obtained in some cases, depending on the performance of our electron spectrometer. Presently there exist no theoretical calculations for DDCS's of this type and range.

II. EXPERIMENT

Our spectrometer is comprised of single hemispherical energy selectors for the primary electron beam and the scattered electron analyzer as described in Childers *et al.* [5,27], where it was used to investigate the electron-impact ionization of H, and in [6,8], where it was used for investigating the electron-impact ionization of He and Ne,Xe, respectively. This spectrometer operated at an electron current of 50–100 nA with a resolution of ≈140 meV. The electron beam crossed an effusive source of gas emitted by a 2.5-cm-long molybdenum needle of inner and outer diameters of 1 and 1.3 mm, respectively. Shielding surfaces around the collision region (including the needle) were grounded and sooted with an acetylene flame to suppress

the production of secondary electrons by the primary electron beam colliding with these surfaces. The depth of field of the scattered electron analyzer was restricted to a small region around the collision center (5–6 mm region) by using an additional pupil in the input electron lens stack of the detector. The spectrometer was baked to greater than 120 °C to improve the stability of the electron beam and the detector and was housed in a double μ-metal shield system that reduced the ambient magnetic field at the collision region to below 5 mG.

The molybdenum needle was incorporated into a moveable gas target source [28]. Using the moveable source setup, it was possible expediently to obtain background-free electron-energy-loss spectra. This enabled us to determine the electron counts under discrete excitation peaks as well as under the ionization continuum via a 1:1 simple subtraction. The tip of the needle was kept 5 mm below the center of the collision region. At $\theta \leqslant 10^\circ$, at lower-$E_0$ values and low E_R, we observed an additional source of secondary electrons systematically affecting our background subtraction, which suggests to us that the small electron beam changed size (due to space-charge neutralization) at the collision region when the gas beam was moved into and out of alignment. This affects the small-angle data more because of the increased electron-gas beam overlap region at small scattering angles. This effect produced an additional source of secondary electrons from the analyzer shielding plates' area where the primary beam was hitting (E_R below 1 eV) that could not be systematically removed by subtracting the electron-energy-loss spectra with the gas in and out of alignment with the incident electron beam. These spectra were therefore not included in the data sets, which start at $\theta = 15^\circ$ in most of the E_0 values here, except for Ar at 30 eV.

We calibrated the transmission of our analyzer using He as a target as follows. First, the detector transmission was arranged to be as uniform as possible for electrons with different E_R values by tuning the analyzer and monitoring the flatness of the helium continuum at $E_0 \approx 30$ eV and $\theta = 90^\circ$. The fact that the helium continuum energy-loss spectrum is "flat" was established by Pichou *et al.* [29] and reconfirmed later by us with atomic hydrogen as a standard [27]. At larger E_R values in our experiment (typically exceeding 1 eV), the transmission response of the spectrometer was found to be stable during the course of measurements as long as the analyzer was not retuned. However, closer to zero E_R around 0.5 eV this uniform transmission could not be achieved as reliably as at higher E_R values, and this added to the errors to our DDCS's at small E_R. We were also limited to a minimum $E_R \approx 0.7$ eV since the spectrum at these low-E_R values was centered around a secondary electron peak that did not always subtract out properly; see Fig. 1 for sample spectra taken for Ar and Kr. We note that baking the spectrometer (electron gun, analyzer, and collision region) stabilized the transmission of the instrument. These transmission calibrations were all performed at $E_0 = 30$ eV for $\theta = 90^\circ$. This calibration provides for a 5.4 eV E_R (continuum) window to calibrate the low-E_R electrons (the ionization potential of He is 24.6 eV). This range can be extended further by including the excitation of the $n = 2$ states of He to an increased E_R window of 8.8 eV.

For those spectra taken at impact energies so the E_R of the ionized electrons exceeded 8.8 eV, the transmission outside this range was initially flat-extrapolated as it could not be measured. However, we generally found that simply extending beyond this E_R window did not accurately correct for the transmission in the extrapolated region, and an exponential function was used (based on the extreme high E_R end of the He-based transmission data) that would converge asymptotically to a flat transmission at large E_R. Using this procedure, the integrated TICS's agreed within uncertainties with those available in the literature.

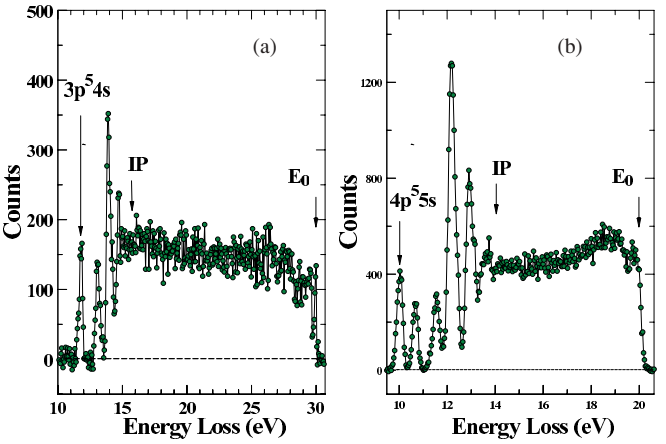

FIG. 1. (Color online) Background subtracted electron-energy-loss spectra of (a) Ar taken at $E_0 = 30$ eV and $\theta = 70^\circ$ and (b) Kr taken at $E_0 = 20$ eV and $\theta = 90^\circ$.

Having determined the transmission of the spectrometer, we measured electron-energy-loss spectra of Ar and Kr at several selected E_0 values in the range below the second-ionization threshold of these gases for scattering angles of 10° to 120°, mostly in 10° intervals. Samples of these spectra are shown in Fig. 1. As in our previous work [6,8] from the continuum energy-loss spectra of the ionization region, we determined normalized DDCS's by the equation

$$\frac{d^2\sigma_X(E_0,E,\theta)}{d\Omega dE} = \frac{N(E,\text{continuum})}{N(X)\Delta E}\frac{d\sigma_X(E_0,E,\theta)}{d\Omega} \qquad (2)$$

where $N(E$,continuum) is the height of the continuum (number of electron scattering events) at the position E (electron energy loss) in the continuum, ΔE (typically set to ≈0.04 eV) is the energy-loss step width per channel in the energy-loss spectrum, $N(X)$ is the total number of electron scattering events under the summed, discrete energy-loss features for the target X, and $d\sigma_X/d\Omega$ is the differential cross section (DCS) from Table I for the excitation of these summed energy-loss features from [30–32]. The value of $N(E$, continuum) was determined by fitting the ionization energy-loss continuum to a polynomial series in E of order $\geqslant 2$. The calibration of the spectrum was dependent upon an accurate determination of the value of ΔE. This value was determined from the energy-loss spectra in which the starting energy-loss and ending energy-loss values were recorded. The incident energy of the electron beam was determined from the spectrum by using the high-end cutoff energy-loss value (see Fig. 1) of the continuum. This method served to determine E_0 to an accuracy of ±0.15 eV. The quoted E_0 values in our DDCS's are an average of these measurements.

TABLE I. Values of DCS's (used in this work for normalization) for the electron-impact excitation of (a) Ar summed levels of the $2p^5 3s$ configuration and (b) the summed $4p^5 6s$ configuration of Kr used. Units are 10^{-19}cm^{2}sr^{-1}. See text for discussion.

	E_0 (eV)			
θ (deg)	17 eV	18 eV	20 eV	30 eV
		(a)		
10				588
15	51.9	69.9	102.2	291
20	32.8	41.4	59.0	129
25	22.1	26.3	43.6	73.6
30	17.3	20.3	33.6	51.6
35	15.8	18.8	28.7	39.5
40	16.6	20.3	26.7	27.5
50	20.7	27.0	25.0	14.7
60	22.5	27.8	24.0	7.87
70	27.2	28.6	25.4	4.88
80	18.6	17.4	20.6	4.13
90	9.14	12.4	13.9	4.20
100	11.1	13.4	12.2	4.19
110		9.4	17.4	4.16
120		4.1	30.6	4.21
Error %	15.5	15.2	14.9	12.9
	E_R (eV)			
θ (deg)	15 eV	16 eV	17.5 eV	20 eV
		(b)		
15	84.8	106	134	200
20	60.4	66.6	84.0	134
25	43.2	41.0	52.9	95.8
30	33.2	28.0	37.0	74.4
35	28.7	23.8	30.9	61.6
40	27.2	24.5	30.1	53.0
50	26.3	29.1	34.1	41.9
60	23.3	29.9	36.5	35.8
70	18.3	25.1	32.3	30.2
80	13.8	17.7	22.5	22.5
90	12.3	12.6	13.6	15.5
100	14.5	13.2	12.5	14.1
110	18.5	18.5	19.6	18.5
120	21.4	24.3	28.7	24.5
Error %	12.5	14.0	13.8	13.8

The spectra were corrected for the transmission of the spectrometer and then normalized to the summed DCS's for electron-impact excitation of the Ar $3p^5 4s$ configuration from the recent work of [30] for $E_0 \leqslant 20$ eV and using the DCS's from our earlier measurements [31] for $E_0 = 30$ eV. For Kr, we normalized to the summed DCS's for the excitation of the Kr $4p^5 5s$ configuration from [32] and the B-spline R-matrix calculations incorporated with recent experimental DCS's [33], which shows excellent relative shape agreement with [32] for all the fine-structure states. Interpolation between DCS's for E_0 values of 17 and 18 eV for Ar were obtained by linearly interpolating the DCS's in [30] at $E_0 = 16.75, 17$, and 20 eV. For Kr, for E_0 values of 16 and 17.5 eV, we used theoretical DCS's from [33] as the theory in [33] showed good agreement with the DCS's of [32] at $E_0 = 15$ and 20 eV, and so we should be in good agreement at energies in between.

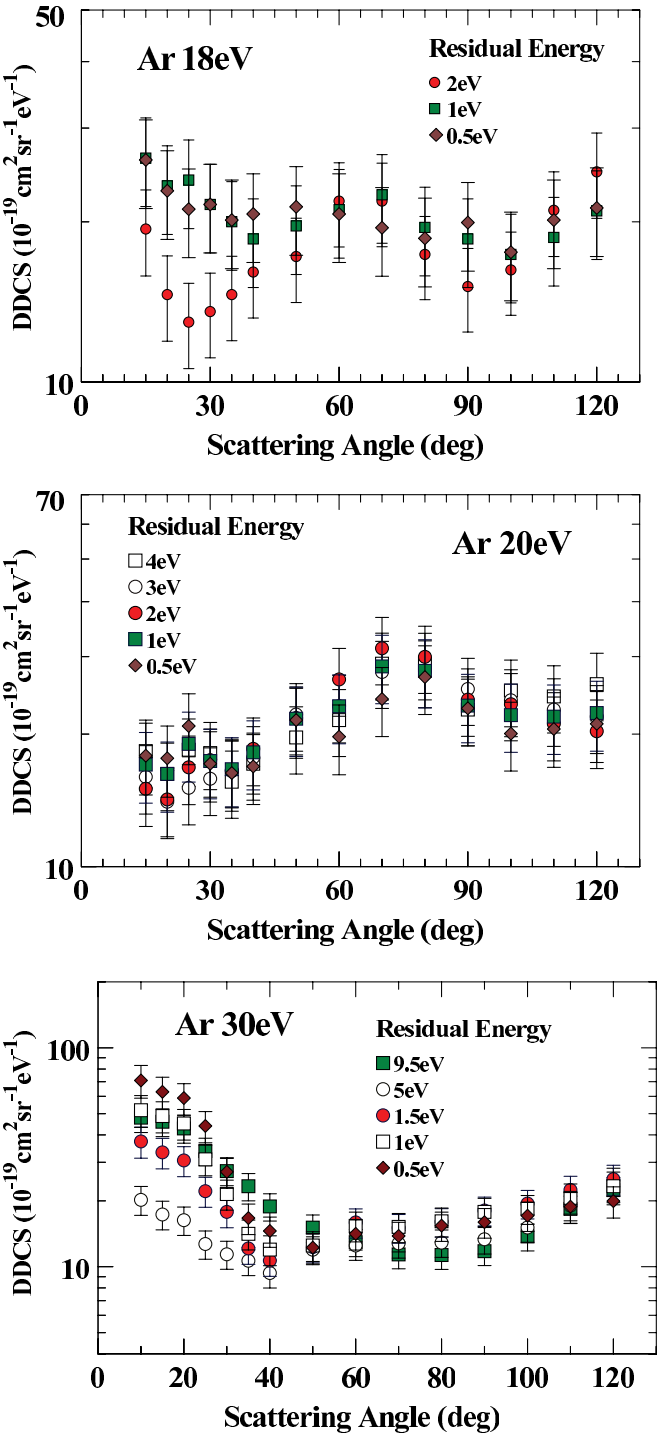

FIG. 2. (Color online) DDCS's for electron-impact ionization of Ar at different E_0 values and for several selected residual energies E_R.

Our DDCS's were extrapolated to small and large scattering angles and then integrated over all scattering angles to obtain singly differential cross sections (SDCS). These SDCS's were then integrated over E_R and divided by 2 (to account for the scattered electron only) to obtain TICS's. Our TICS's were finally normalized onto an absolute scale to those of Rapp and Englander-Golden [13] for Ar and Kr, and the normalization factor was satisfactorily within 25% from unity on average. In

TABLE II. Present DDCS's and SDCS's for the electron-impact ionization of Ar. (a) $E_0 = 17$ eV; (b) $E_0 = 18$ eV; (c) $E_0 = 20$ eV; and (d) $E_0 = 30$ eV. Units: DDCS's: 10^{-19} cm^2 sr^{-1} eV^{-1}; SDCS: 10^{-19} cm^2 eV^{-1}.

	E_R (eV)					
	1		0.5		0.3	
θ (deg)	DDCS	Error	DDCS	Error	DDCS	Error
			(a)			
15	22.1	4.6	20.7	4.6	20.7	5.0
20	19.9	4.1	20.0	4.2	19.9	4.2
25	21.0	3.9	21.9	4.3	20.4	4.3
30	21.3	3.9	20.4	3.9	19.1	3.9
35	20.2	3.7	18.8	3.6	21.1	4.2
40	19.4	3.5	18.4	3.5	19.2	3.8
50	17.5	3.2	19.2	3.6	19.6	3.9
60	16.3	2.9	16.1	3.0	17.9	3.6
70	17.1	3.1	20.9	3.9	16.8	3.3
80	17.7	3.2	17.3	3.2	18.1	3.5
90	16.9	3.0	18.8	3.5	17.0	3.4
100	17.4	3.1	18.2	3.4	16.8	3.3
SDCS	212	41	214	43	222	45

	E_R (eV)									
	2		1.5		1		0.5		0.3	
θ (deg)	DDCS	Error	DDCS	Error	DDCS	Error	DDCS	Error	DDCS	Error
					(b)					
15	19.39	3.57	16.55	3.14	26.36	4.99	26.14	4.95	17.13	3.25
20	14.59	2.66	14.59	2.77	23.36	4.43	22.87	4.33	16.76	3.17
25	12.96	2.36	13.49	2.56	23.96	4.54	21.13	4.00	21.29	4.03
30	13.56	2.45	13.56	2.57	21.56	4.09	21.56	4.09	21.75	4.12
35	14.59	2.64	14.59	2.77	20.01	3.79	20.15	3.82	21.75	4.12
40	16.10	2.90	16.10	3.05	18.57	3.52	20.69	3.92	19.44	3.68
50	17.21	3.10	17.21	3.26	19.65	3.72	21.35	4.04	18.51	3.51
60	21.88	3.94	21.88	4.15	21.08	4.00	20.69	3.92	20.37	3.86
70	21.87	3.91	22.17	4.20	22.49	4.26	19.49	3.69	23.14	4.39
80	17.37	3.09	17.37	3.29	19.53	3.70	18.62	3.53	22.22	4.21
90	15.12	2.70	15.12	2.86	18.57	3.52	19.93	3.78	25.92	4.91
100	16.24	2.90	16.24	3.08	17.37	3.29	17.53	3.32	18.51	3.51
110	21.02	3.81	21.02	3.98	18.69	3.54	20.15	3.82	20.37	3.86
120	24.83	4.53	24.83	4.71	20.96	3.97	21.24	4.02	21.75	4.12
SDCS	262	46	261	47	260	49	262	51	267	54

	E_R (eV)													
	4		3		2		1.5		1		0.5		0.3	
θ (deg)	DDCS	Error	DDCS	Error	DDCS	Error	DDCS	Error	DDCS	Error	DDCS	Error	DDCS	Error
							(c)							
15	18.3	3.2	16.0	2.8	15.0	2.7	14.3	2.6	17.1	3.1	17.9	3.3	20.5	3.9
20	16.2	2.8	14.0	2.5	14.2	2.5	15.1	2.7	16.2	2.9	17.6	3.2	19.7	3.7
25	18.4	3.2	15.1	2.7	16.8	3.0	17.8	3.2	19.0	3.4	20.9	3.8	19.9	3.7
30	18.1	3.2	15.8	2.8	17.5	3.1	18.2	3.2	17.4	3.1	17.1	3.1	16.9	3.1
35	15.6	2.7	16.5	2.9	16.6	2.9	16.9	3.0	16.6	3.0	16.3	3.0	19.9	3.7
40	17.1	3.0	17.7	3.1	18.5	3.3	18.3	3.2	18.2	3.3	16.9	3.1	17.9	3.3
50	19.7	3.4	22.2	3.9	21.8	3.8	21.5	3.8	21.7	3.9	21.5	3.9	20.3	3.7
60	21.5	3.7	23.1	4.0	26.6	4.7	25.9	4.6	23.1	4.1	19.7	3.6	21.0	3.8
70	28.9	5.0	27.7	4.8	31.3	5.5	29.8	5.2	28.5	5.0	24.0	4.3	25.2	4.6
80	28.9	5.0	27.8	4.8	30.0	5.2	29.2	5.1	27.9	4.9	27.0	4.8	26.5	4.8
90	22.7	3.9	25.3	4.4	24.0	4.2	24.7	4.3	23.2	4.1	22.9	4.1	23.1	4.2
100	25.1	4.3	23.9	4.1	23.4	4.1	22.9	4.0	22.1	3.9	20.1	3.6	21.0	3.8
110	24.4	4.2	22.7	4.0	21.1	3.7	22.3	4.0	21.9	3.9	20.5	3.7	22.2	4.1
120	26.0	4.5	21.9	3.9	20.3	3.6	21.1	3.8	22.3	4.0	21.1	3.9	22.6	4.2
SDCS	297	51	299	53	297	54	294	55	295	57	291	58	287	59

TABLE II. (*Continued*)

	E_R (eV)											
	14		12.5		11		9.5		8		6.5	
θ (deg)	DDCS	Error	DDCS	Error	DDCS	Error	DDCS	Error	DDCS	Error	DDCS	Error
						(d)						
10	112.3	16.0	83.3	11.9	63.9	9.2	48.0	7.0	38.7	5.7	27.1	4.0
15	91.1	12.9	72.8	10.4	58.3	8.4	45.9	6.6	36.2	5.3	24.4	3.6
20	69.7	9.8	55.9	7.9	50.0	7.1	42.8	6.2	33.7	4.9	22.9	3.4
25	48.4	6.8	44.2	6.3	39.5	5.6	33.8	4.8	26.4	3.8	18.9	2.8
30	40.8	5.7	37.5	5.3	33.2	4.7	27.3	3.9	21.4	3.1	15.8	2.3
35	34.2	4.8	30.7	4.3	27.6	3.9	23.3	3.3	18.6	2.7	14.2	2.1
40	25.8	3.6	23.2	3.3	21.0	3.0	18.8	2.7	15.5	2.2	12.9	1.9
50	19.6	2.7	17.3	2.4	16.4	2.3	15.1	2.1	13.8	2.0	12.7	1.8
60	15.4	2.2	14.0	2.0	13.5	1.9	13.0	1.8	12.5	1.8	12.4	1.8
70	12.5	1.7	11.8	1.7	11.2	1.6	11.4	1.6	11.5	1.6	12.0	1.7
80	12.8	1.8	11.8	1.6	11.1	1.6	11.3	1.6	11.2	1.6	11.9	1.7
90	14.4	2.0	12.7	1.8	12.4	1.7	11.8	1.7	11.8	1.7	12.4	1.8
100	15.4	2.1	15.5	2.2	14.3	2.0	13.7	1.9	13.4	1.9	14.0	2.0
110	18.5	2.6	17.6	2.5	17.5	2.5	18.4	2.6	17.6	2.5	18.5	2.7
120	20.4	2.9	20.2	2.9	20.9	3.0	22.4	3.2	23.5	3.4	24.3	3.5
SDCS	284	41	261	38	256	37	252	37	241	35	237	34

	E_R (eV)											
	5		3.5		2.5		2		1.5		1		0.5	
θ (deg)	DDCS	Error	DDCS	Error	DDCS	Error	DDCS	Error	DDCS	Error	DDCS	Error	DDCS	Error
							(d)							
10	20.2	3.0	17.8	2.7	18.0	2.8	20.8	3.3	37.4	6.0	51.9	8.6	236.5	40.2
15	17.3	2.6	12.5	1.9	14.5	2.2	16.4	2.6	33.3	5.3	48.8	7.9	209.7	35.0
20	16.3	2.4	11.4	1.7	13.0	2.0	15.1	2.3	30.6	4.8	45.1	7.2	196.5	32.1
25	12.7	1.9	8.98	1.34	12.9	1.9	14.9	2.3	22.1	3.5	31.0	4.9	146.5	23.9
30	11.4	1.7	9.70	1.43	11.7	1.7	13.5	2.1	17.8	2.7	21.5	3.4	90.5	14.5
35	10.7	1.6	8.09	1.19	8.25	1.23	9.78	1.48	12.1	1.9	14.1	2.2	55.6	8.8
40	9.36	1.36	8.17	1.20	8.03	1.19	8.99	1.35	10.7	1.6	12.0	1.9	48.5	7.7
50	12.0	1.7	11.3	1.7	11.0	1.6	11.7	1.8	12.3	1.9	12.5	1.9	40.8	6.5
60	12.5	1.8	12.8	1.9	13.0	1.9	14.3	2.1	15.9	2.4	15.4	2.4	47.1	7.4
70	12.8	1.8	13.1	1.9	13.2	1.9	14.2	2.1	15.1	2.3	15.2	2.3	46.1	7.1
80	12.9	1.8	13.6	2.0	14.0	2.0	15.0	2.2	16.0	2.4	16.1	2.4	51.4	7.8
90	13.3	1.9	15.0	2.2	15.6	2.3	16.8	2.5	18.1	2.7	17.8	2.7	53.2	8.2
100	15.1	2.2	17.0	2.5	17.7	2.6	19.0	2.8	19.4	2.9	18.4	2.8	57.0	8.7
110	19.0	2.8	21.4	3.2	20.7	3.1	21.6	3.3	22.4	3.5	20.6	3.2	62.7	10.0
120	24.6	3.6	25.1	3.8	24.0	3.6	24.8	3.8	25.1	3.9	23.3	3.7	66.4	10.8
SDCS	241	35	244	35	247	36	259	38	265	38	267	39	278	40

the determination of our SDCS's (via solid-angle integration of our DDCS's), we visually extrapolated our DDCS's to small and large scattering angles outside of the experimental scattering range. The error in this extrapolation was estimated by repeating this integration, but instead employing flat DDCS extrapolations to $\theta = 0^\circ$ and 180° from the end points of the angular distribution of the DDCS's. The error estimate was determined from the difference of the two extrapolations and added in quadrature with the mean error of our DDCS's. The SDCS's are expected to be symmetric about the middle of the ionization continuum at the residual energy of $E_R = (E_0 - E_I)/2$, where E_I is the first-ionization energy since the scattered and the total energy of the ionized electron pair (E_P) equals $E_0 - E_I$, provided E_0 is below the second-ionization energy, i.e., only two free electrons result from the post-collision system. This symmetry property of the SDCS about the equal sharing E_R provides a further check on the determination of our He transmission correction procedure that was applied to the experimental energy-loss spectra. We note here that the procedure for normalizing to the TICS of [13] will not be reliable for energies above the second IP, and in this work the only E_0 value above the second IP is that of Ar at 30 eV. However, the normalizing factor between integrating our DDCS's to obtain the TICS's of [13] was close to unity, i.e., 0.785 ± 0.114. Hence our absolute DDCS measurements at 30 eV should be reliable.

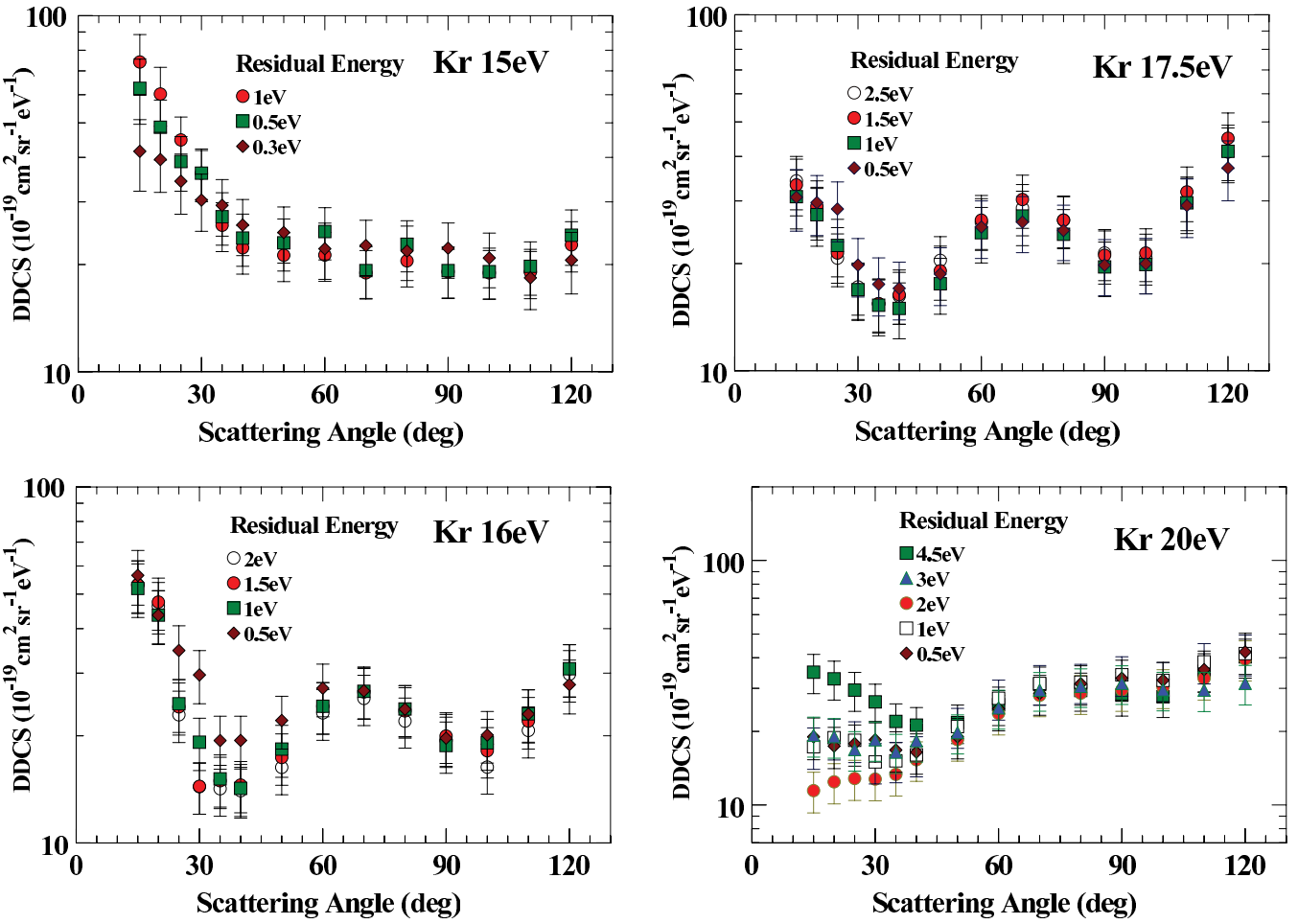

FIG. 3. (Color online) Same as Fig. 2, but for Kr.

III. RESULTS AND OBSERVATION

The resulting DDCS's for Ar and Kr are listed Tables II and III together with SDCS's determined in our analysis of the data. The uncertainties of the DDCS's include those of the inelastic DCS's used for normalization from [30–33] (12.5%–15.5%, see Table I), the uncertainty in the spectrometer transmission (5%–10%), and statistical errors (2%–9%) from determining the background-free continuum signal. Selected DDCS's for Ar are plotted in Fig. 2 and for Kr in Fig. 3. SDCS's for Ar and Kr are plotted in Fig. 4.

The DDCS's for Ar at $E_0 = 17$ eV are not plotted, but are essentially flat, i.e., the distribution of ionized electrons is isotropic, with a small forward-scattering component [see also Table II(a)]. This distribution (at the energy of 1.24 eV above the IP, which is shared between the two electrons) is the flattest of the rare-gas targets previously investigated, including He [6]. This somewhat suggests strong s-wave contributions in the continuum, with minor interaction from the polarization potential of the ionized core. This flat distribution is to some extent supported by the perpendicular-plane (e,2e) results of Nixon *et al.* [14] at an even higher energy E_0 of 2 eV above the IP. However, the in-plane (e,2e) results of Selles *et al.* [12] for Ar show sharp minima structure in the equal-energy sharing distributions at 1 eV above the IP and thus make such comparisons between our results and those of the (e,2e) experiments unclear.

For Ar at $E_0 = 18$ eV, Fig. 2, the distributions are prominently d-type (displaced to smaller θ of 30° and 110°), which is pronounced for the faster, higher E_R electrons and washes out for the slower, lower E_R electrons. For both $E_0 = 17$ and 18 eV, we do not observed any suppression of slow electrons being emitted in the forward direction as was observed for Ne in our previous work [6]. At $E_0 = 20$ eV, the distribution is significantly different from 18 eV. The minima observed at 18 eV at around 30° and 110° are no longer distinct, and a broad peak is seen at 70° for all residual energies.

For $E_0 = 30$ eV (near but above the second IP for Ar) in Fig. 2, the distributions are forward-peaked. The strength of the forward peak when compared to the more pronounced forward scattering in Ne in [6] suggests that the dipole potential is not prominent, or perhaps not as forward aligned by the collision as it is in Ne. The forward peak is more pronounced for the fast and slow electrons and less for the midrange electrons. This likely suggests a more complicated picture involving spin-orbit effects in the core and movement of the polarization of the core in the post-collision regime. PCI effects will strongly affect the emission of the ionized electrons.

TABLE III. Present DDCS's and SDCS's for the electron-impact ionization of Kr. (a) $E_0 = 15$ eV; (b) $E_0 = 16$ eV; (c) $E_0 = 17.5$ eV; (d) $E_0 = 20$ eV. Units are the same as for Table II.

	E_R (eV)					
	1		0.5		0.3	
θ (deg)	DDCS	Error	DDCS	Error	DDCS	Error
			(a)			
15	74.1	14.4	62.5	13.0	41.6	9.5
20	60.3	11.4	48.6	9.3	39.5	7.6
25	44.8	7.2	38.9	6.8	34.3	6.6
30	36.1	5.7	36.1	6.1	30.3	5.5
35	25.8	4.0	27.2	4.6	29.3	5.3
40	22.3	3.5	23.7	4.0	25.8	4.6
50	21.2	3.3	23.0	3.8	24.6	4.4
60	21.3	3.3	24.7	4.1	22.2	4.0
70	18.9	3.0	19.2	3.2	22.6	4.0
80	20.5	3.2	22.8	3.7	21.8	3.8
90	19.1	3.0	19.2	3.2	22.2	3.9
100	18.9	2.9	19.1	3.1	20.9	3.6
110	19.0	3.0	19.8	3.4	18.4	3.4
120	22.7	3.7	24.2	4.3	20.6	4.0
SDCS	322	58	326	64	304	65

	E_R (eV)									
	2		1.5		1		0.5		0.3	
θ (deg)	DDCS	Error	DDCS	Error	DDCS	Error	DDCS	Error	DDCS	Error
					(b)					
15	53.1	8.8	53.1	9.0	51.9	8.9	56.4	9.9	50.9	9.1
20	46.3	7.6	47.5	7.9	43.6	7.4	43.6	7.5	42.9	7.6
25	22.9	3.8	24.1	4.0	24.6	4.2	34.7	6.0	33.0	5.8
30	14.4	2.4	14.4	2.4	19.2	3.2	29.7	5.0	25.1	4.4
35	14.2	2.3	14.9	2.5	15.1	2.5	19.4	3.3	17.4	3.0
40	14.0	2.3	14.5	2.4	14.2	2.4	19.4	3.3	19.9	3.4
50	16.3	2.7	17.4	2.9	18.3	3.1	22.1	3.7	18.5	3.2
60	23.2	3.8	24.2	4.0	24.2	4.0	27.2	4.6	24.0	4.1
70	25.5	4.1	26.6	4.3	26.7	4.4	26.8	4.5	25.2	4.3
80	22.0	3.5	23.5	3.8	23.8	3.9	23.8	3.9	21.9	3.7
90	19.4	3.1	20.0	3.2	18.8	3.1	19.7	3.3	17.6	3.0
100	16.3	2.6	18.2	2.9	19.1	3.1	20.1	3.3	18.1	3.0
110	20.7	3.4	22.0	3.6	23.0	3.9	23.0	3.9	21.3	3.7
120	29.8	4.9	30.9	5.2	30.9	5.2	27.8	4.8	25.5	4.5
SDCS	346	64	364	69	367	70	353	69	349	69

	E_R(eV)															
	3.5		3		2.5		2		1.5		1		0.5		0.3	
θ (deg)	DDCS	Error	DDCS	Error	DDCS	Error	DDCS	Error	DDCS	Error	DDCS	Error	DDCS	Error	DDCS	Error
								(c)								
15	36.1	5.9	35.7	6.0	34.2	5.8	34.1	6.0	33.3	6.0	30.8	5.8	30.7	6.0	30.9	6.4
20	29.2	4.8	28.8	4.8	28.0	4.7	29.7	5.2	29.0	5.2	27.4	5.1	29.7	5.7	29.4	5.9
25	21.3	3.5	21.3	3.5	20.7	3.5	21.3	3.7	21.4	3.8	22.5	4.1	28.5	5.5	28.8	5.8
30	19.0	3.1	18.8	3.1	17.2	2.9	17.2	2.9	16.9	3.0	16.9	3.0	19.8	3.7	21.9	4.3
35	15.4	2.5	15.4	2.5	15.4	2.6	15.4	2.6	15.4	2.7	15.3	2.7	17.5	3.3	19.4	3.8
40	16.3	2.6	16.2	2.7	16.2	2.7	16.2	2.7	16.3	2.8	15.0	2.7	17.0	3.1	17.6	3.4
50	19.8	3.2	19.7	3.2	20.4	3.4	20.2	3.4	19.1	3.3	17.5	3.1	18.7	3.5	18.9	3.6
60	24.6	4.0	25.3	4.1	26.1	4.3	26.6	4.5	26.5	4.6	24.4	4.3	25.3	4.7	24.6	4.7
70	26.5	4.2	28.0	4.5	28.6	4.7	30.3	5.1	30.3	5.2	27.2	4.7	26.2	4.7	25.3	4.7
80	25.6	4.1	25.9	4.2	26.5	4.3	26.5	4.4	26.5	4.5	24.2	4.2	24.8	4.4	25.5	4.7

TABLE III. (*Continued*)

	E_R(eV)															
	3.5		3		2.5		2		1.5		1		0.5		0.3	
θ (deg)	DDCS	Error	DDCS	Error	DDCS	Error	DDCS	Error	DDCS	Error	DDCS	Error	DDCS	Error	DDCS	Error
90	20.3	3.2	20.6	3.3	21.4	3.5	21.8	3.6	21.1	3.6	19.6	3.4	19.8	3.6	19.5	3.6
100	19.0	3.0	19.3	3.1	20.8	3.4	21.3	3.5	21.4	3.6	19.9	3.4	20.0	3.6	19.5	3.6
110	26.3	4.3	26.9	4.4	29.7	5.0	31.8	5.4	31.8	5.6	29.6	5.4	29.1	5.5	27.6	5.4
120	36.1	5.9	37.7	6.3	41.1	7.0	43.4	7.5	45.0	8.0	41.3	7.6	37.1	7.1	32.8	6.6
SDCS	371	63	376	65	391	68	408	71	415	73	395	71	377	68	374	68

	E_R (eV)											
	6.0		5.5		5.0		4.5		4.0		3.5	
θ (deg)	DDCS	Error	DDCS	Error	DDCS	Error	DDCS	Error	DDCS	Error	DDCS	Error
						(d)						
15	40.9	7.4	40.1	7.2	33.3	6.1	34.9	6.4	27.8	5.1	21.4	4.0
20	38.1	6.8	37.2	6.7	32.7	5.9	32.8	5.9	26.5	4.8	20.7	3.8
25	36.0	6.4	34.8	6.2	30.3	5.5	29.5	5.3	27.9	5.1	20.1	3.7
30	34.0	6.1	32.4	5.8	28.9	5.2	26.4	4.8	28.0	5.1	18.5	3.4
35	27.9	5.0	27.2	4.9	25.8	4.6	21.9	3.9	28.4	5.1	18.9	3.4
40	23.2	4.1	23.9	4.3	25.2	4.5	21.2	3.8	28.2	5.1	19.1	3.5
50	24.3	4.3	24.1	4.3	21.4	3.8	21.7	3.9	31.5	5.7	20.9	3.8
60	27.3	4.8	26.9	4.8	25.0	4.5	25.7	4.6	34.2	6.1	26.2	4.7
70	28.7	5.1	28.1	5.0	26.1	4.6	31.1	5.5	32.0	5.7	28.9	5.2
80	30.5	5.4	29.4	5.2	27.9	4.9	29.4	5.2	26.3	4.7	30.9	5.5
90	28.8	5.1	29.5	5.2	28.5	5.1	28.1	5.0	25.9	4.6	29.4	5.3
100	28.0	4.9	28.8	5.1	28.9	5.1	27.7	4.9	26.1	4.6	28.7	5.1
110	36.1	6.4	35.5	6.3	35.8	6.4	35.2	6.3	31.5	5.7	30.2	5.5
120	44.1	7.9	42.8	7.7	37.5	6.8	40.3	7.3	35.6	6.5	32.8	6.0
SDCS	453	79	446	79	410	73	417	75	402	72	373	68

	E_R (eV)													
	3.0		2.5		2.0		1.5		1.0		0.5		0.3	
θ (deg)	DDCS	Error	DDCS	Error	DDCS	Error	DDCS	Error	DDCS	Error	DDCS	Error	DDCS	Error
							(d)							
15	19.3	3.6	15.0	2.8	11.4	2.2	12.7	2.4	17.3	3.3	19.0	3.7	17.2	3.4
20	19.0	3.5	14.2	2.6	12.4	2.3	13.1	2.5	18.8	3.6	17.4	3.3	18.2	3.5
25	16.8	3.1	14.3	2.7	12.8	2.4	13.0	2.4	18.4	3.5	17.8	3.4	19.0	3.7
30	18.5	3.4	15.3	2.8	12.8	2.4	13.5	2.5	15.0	2.8	18.5	3.5	19.8	3.8
35	16.4	3.0	14.3	2.6	13.3	2.5	13.3	2.5	15.2	2.8	16.8	3.2	18.1	3.4
40	18.3	3.3	15.7	2.9	15.3	2.8	16.1	3.0	16.0	3.0	16.4	3.1	16.4	3.1
50	19.8	3.6	19.0	3.5	18.5	3.4	18.8	3.5	20.9	3.9	19.0	3.6	18.9	3.6
60	24.9	4.5	27.9	5.1	23.7	4.3	22.7	4.2	27.3	5.1	24.7	4.6	24.5	4.6
70	29.5	5.3	32.2	5.8	28.1	5.1	29.7	5.4	31.4	5.8	28.6	5.3	28.2	5.3
80	30.5	5.5	31.5	5.7	28.6	5.2	30.7	5.6	31.8	5.8	31.3	5.8	30.5	5.6
90	31.4	5.7	32.2	5.8	29.5	5.4	34.3	6.3	34.1	6.3	33.0	6.1	32.4	6.0
100	29.6	5.3	31.2	5.6	30.2	5.5	32.7	6.0	32.3	5.9	32.4	6.0	38.5	7.1
110	29.5	5.4	30.0	5.5	32.9	6.1	39.0	7.3	38.5	7.2	35.8	6.8	39.8	7.6
120	31.4	5.8	31.3	5.8	39.5	7.4	42.9	8.1	41.6	7.9	42.3	8.1	44.4	8.6
SDCS	369	67	369	68	389	72	419	78	428	80	422	80	433	82

For Kr, Fig. 3, the DDCS distributions are forward peaked at $E_0 = 15$ eV, about 1 eV above the IP for essentially all scattered electrons even for $E_R = 0.3$ eV. However, at $E_0 = 16$ eV, the situation is changed with a *d*-type distribution superimposed on a strong forward-scattered one. The *d*-type distribution persists at $E_0 = 17.5$ eV, in fact being more pronounced at this energy. At $E_0 = 20$ eV, the forward scattering is significantly reduced in an almost similar way as for Ar, but the distributions are complicated. However, we note a similarity in these distributions between Kr and Ar at

$E_0 = 20$ eV, much more than for any of the other rare gases. We note that similar d-type distributions for Kr at $E_0 = 17.5$ eV were observed previously for Xe at 14 eV.

In Fig. 4, we display the SDCS's from our work. Here, we have shown the relative errors, i.e., not including the errors due to normalization to the inelastic DCS used. For both Ar and Kr, at lower-E_0 values, we are not able to resolve the weak curvature of the distributions, which look flat. However, for the highest E_0 covered here, i.e., Ar at $E_0 = 30$ eV and Kr at 20 eV, we see that the distributions are concave, or smile-type distributions, similar to Xe but opposite to that of Ne. Here, this consideration of Ar at 30 eV has to be done with some care, as this energy is above its second IP and means that 3-electrons are involved. However, the third-electron emission could be a perturbative correction to a two-electron emission at this E_0 value, which is only 2.37 eV above the second IP. When our overall SDCS results are compared for all the rare gases, we see that Ne is the odd one out. Ne shows a marked anomaly among the rare gases when one compares the values of TICS's for the rare gases as a function of energy. From Fig. 5, we see that, e.g., at about 1 eV above its IP, the TICS's of Ne are in fact about 30% lower than He, where one would expect them to be higher, whereas Ar has a TICS that is about five times that of He at 1 eV above its IP, Kr is about 10 times, and Xe is about 20 times. If one examines this surprising progression, the TICS of Ne should be three times what it is close to threshold. In fact, the TICS of Ne remains "suppressed" so that only at about 9.3 eV above its IP is it equal to that of He, but it remains significantly below Ar, Kr, and Xe, only "catching up" at energies of 30 eV above its IP. In this region, multielectron ionization effects will complicate the picture. This anomaly may likely have some bearing on the overall energy sharing of the two electrons, as well as being caused (to a large extent) by the polarization potential of the $^2P_{1/2,3/2}$ ionized core. As mentioned before, only in Ne [8] did we observe a strong suppression of low E_R electrons emitted in the forward-scattering direction at low E_0, especially closest to threshold. The other rare gases do not show this as significantly, although their core structure is essentially the same. It is possible that the role of spin-orbit coupling modifies (reduces) the overall dominance of the core polarization potential, making it easier for these low E_R electrons at near threshold to escape. Unfortunately, our DDCS data are limited because of their error uncertainties in tracking the shape of the SDCS (when solid-angle integrated) especially closer to threshold.

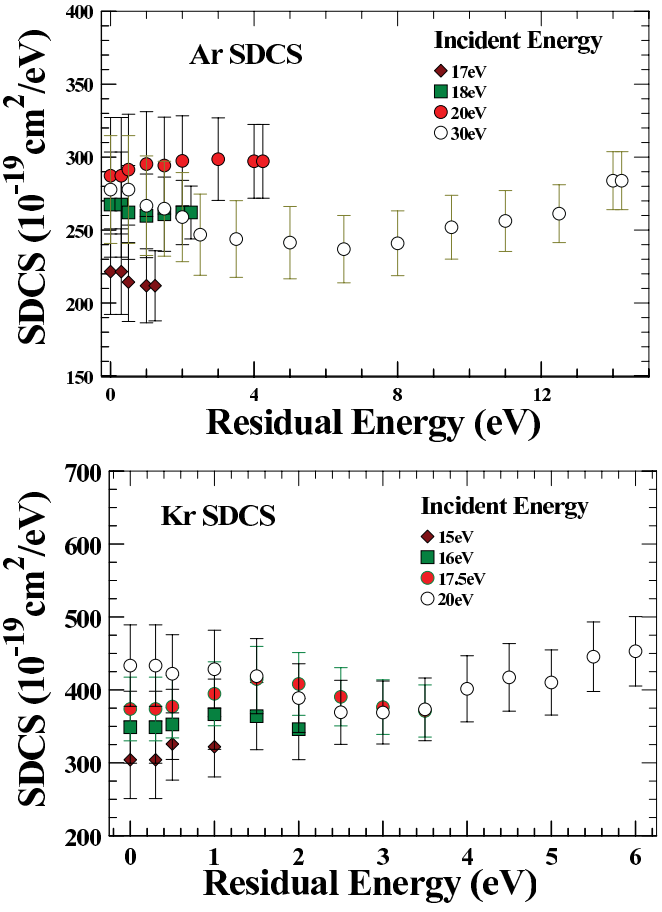

FIG. 4. (Color online) Present SDCS's for Ar and Kr at different incident energies with relative (shape) errors plotted. See text for discussion.

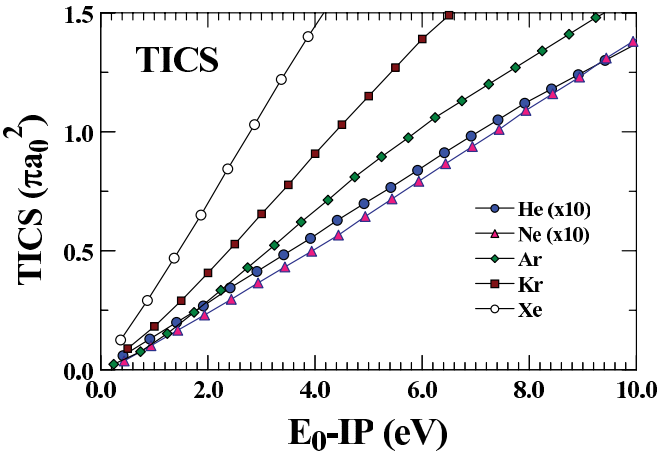

FIG. 5. (Color online) TICS's for the rare gases as a function of incident excess energy above the IP from Rapp and Englander-Golden [13]. The TICS's of He and Ne have been scaled up by a factor of 10. See text for discussion.

IV. CONCLUSIONS

Near-threshold measurements of doubly differential cross sections for electron-impact ionization of Ar and Kr are presented. The measurements at these near-threshold energies are made possible by determining a background-free scattered electron signal along the ionization continuum by implementing our moveable source system [28] to obtain normalized quantitative DDCS's for these systems. The results show similarities between Ar and Kr with our earlier Xe DDCS and SDCS [8], which were taken with the same instrument and using the same moveable source technique. However, we find significant differences between Ar and Kr with our earlier Ne DDCS and SDCS. It was difficult to compare our DDCS's with the results from existing (e,2e) measurements in the same near-threshold energy range. However, it is important for theory to enlighten this situation as to how Ne (anomalously)

suppresses its TICS as compared to the other rare gases, which are relatively similar in their DDCS and the shape of their SDCS. Toward this end it would be useful if near-threshold $(e,2e)$ measurements of the kind undertaken by the Manchester group [14] were also taken in-plane to see if the slow E_R suppression hypothesis is correct, as this would shed new light and open up interest in the role of the ionized core's dipole potential in the post-collision process.

ACKNOWLEDGMENTS

This work was funded by the NSF under Grants No. RUI-PHY-0653450 and No. 0965793. Useful and important discussions with Dr. James Colgan (Los Alamos National Laboratory, NM), Dr. Don Madison (Missouri Institute of Technology, Rolla, MO), and Dr. Klaus Bartschat (Drake University, Des Moines, IA) are gratefully acknowledged.

[1] T. N. Rescigno, M. Baertschy, W. A. Isaacs, and C. W. McCurdy, Science **286**, 2474 (1999).
[2] I. Bray and A. T. Stelbovics, Phys. Rev. A **46**, 6995 (1992).
[3] I. Bray and D. V. Fursa, Phys. Rev. A **54**, 2991 (1996).
[4] D. A. Horner, C. W. McCurdy, and T. N. Rescigno, Phys. Rev. A **71**, 012701 (2005).
[5] J. G. Childers, K. E. James Jr., M. Hughes, I. Bray, M. Baertschy, and M. A. Khakoo, Phys. Rev. A **68**, 030702(R) (2003).
[6] E. Schow, K. Hazlett, J. G. Childers, C. Medina, G. Vitug, I. Bray, D. V. Fursa, and M. A. Khakoo, Phys. Rev. A **72**, 062717 (2005).
[7] M. Hughes, K. E. James Jr., J. G. Childers, and M. A. Khakoo, Meas. Sci. Technol. **15**, 841 (2003).
[8] B. Yates, K. Keane, and M. A. Khakoo, J. Phys. B **42**, 095206 (2009).
[9] A. N. Bhoj and M. Kushner, J. Phys. D **37**, 2510 (2004).
[10] R. N. Franklin, J. Phys. D **36**, 2655 (2003).
[11] V. M. Donnelly, Plasma Sci. **28**, 123 (2004).
[12] P. Selles, J. Mazeau, and A. Huetz, J. Phys. B **23**, 2613 (1990).
[13] D. Rapp and P. Englander-Golden, J. Chem. Phys. **43**, 1464 (1965).
[14] K. L. Nixon, A. J. Murray, and C. Kaiser, J. Phys. B **43**, 085202 (2010).
[15] O. Al-Hagan, C. Kaiser, A. J. Murray, and D. H. Madison, Nat. Phys. **5**, 59 (2009).
[16] O. Al-Hagan, A. J. Murray, C. Kaiser, J. Colgan, and D. H. Madison, Phys. Rev. A **81**, 030701(R) (2010).
[17] X. Ren *et al.*, Phys. Rev. A **82**, 032712 (2010).
[18] E. M. Staicu Casagrande, A. Naja, A. Lahmam-Bennani, A. S. Kheifets, D. H. Madison, and B. Joulakian, J. Phys: Conf. Ser. **141**, 012016 (2008).
[19] L. R. Hargreaves, C. Colyer, M. A. Stevenson, B. Lohmann, O. Al-Hagan, D. H. Madison, and C. G. Ning, Phys. Rev. A **80**, 062704 (2009).
[20] B. Rouvellou, S. Rioual, J. Röder, A. Pochat, J. Rasch, C. T. Whelan, H. R. J. Walters, and R. J. Allan, Phys. Rev. A **57**, 3621 (1998).
[21] M. A. Stevenson and B. Lohmann, Phys. Rev. A **77**, 032708 (2008).
[22] M. A. Stevenson and B. Lohmann, Phys. Rev. A **73**, 020701(R) (2006).
[23] A. C. F. Santos, A. Hasan, T. Yates, and R. D. DuBois, Phys. Rev. A **67**, 052708 (2003).
[24] A. C. F. Santos, A. Hasan, and R. D. DuBois, Phys. Rev. A **69**, 032706 (2004).
[25] O. G. de Lucio, J. Gavin, and R. D. DuBois, Phys. Rev. A **75**, 052709 (2007).
[26] R. Rejoub, B. G. Lindsay, and R. F. Stebbings, Phys. Rev. A **65**, 042713 (2002).
[27] J. G. Childers, K. E. James Jr., I. Bray, M. Baertschy, and M. A. Khakoo, Phys. Rev. A **69**, 022709 (2004).
[28] M. Hughes, K. E. James Jr., J. G. Childers, and M. A. Khakoo, Meas. Sci. Technol. **15**, 841 (2003).
[29] F. Pichou, A. Huetz, G. Joyez, and M. Landau, J. Phys. B **11**, 3683 (1978).
[30] M. A. Khakoo, O. Zatsarinny, and K. Bartschat, J. Phys. B **44**, 015201 (2011).
[31] M. A. Khakoo *et al.*, J. Phys. B **37**, 247 (2003).
[32] X. Guo, D. F. Mathews, G. Mikaelian, M. A. Khakoo, A. Crowe, I. Kanik, S. Trajmar, V. Zeman, K. Bartschat, and C. J. Fontes, J. Phys. B **33**, 1895 (2000).
[33] M. Allan, O. Zatsarinny, and K. Bartschat (private communication).